Check for updates

Pulsed turbidite and methane seep records in the north western South China Sea since the last glacial maximum

Jingrui Li[1], Xiaoming Miao[2], Xiuli Feng[2]*, Rui Jiang[1],
Mengwei Zhao[3], Xiaopeng Dan[2], Qianwen Xiao[2]
and Jiangong Wei[4,5,6,7]*

[1]Deep-sea Multidisciplinary Research Center & Laboratory for Marine Geology, Laoshan Laboratory,
Qingdao, China, [2]Key Laboratory of Submarine Geosciences and Prospecting, College of Marine
Geosciences, Ocean University of China, Qingdao, China, [3]Center for Isotope Geochemistry and
Geochronology, Laoshan Laboratory, Qingdao, China, [4]Key Laboratory of Marine Mineral Resources,
Guangzhou Marine Geological Survey, Ministry of Natural Resources, Guangzhou, China, [5]Sanya
Institute of South China Sea Geology, Guangzhou Marine Geological Survey, Sanya, China, [6]Academy
of South China Sea Geological Science, China Geological Survey, Sanya, China, [7]Southern Marine
Science and Engineering Guangdong Laboratory, Guangzhou, China

The small-scale event layers in the continental margin contain abundant
dynamic environment information, and pose a challenge to the interpretation
of continuous sedimentary records, giving geological significance to their
accurate identify and possible genesis. Here, pulsed turbidite layers since the
last glacial maximum (LGM) in a gravity core in the northwestern South China Sea
(SCS) was analyzed to investigate the precisely identification, possible causes and
the role of marine environmental change during the late Quaternary in formation
of these small-scale event layers in the SCS. Eight potential pulsed turbidite
layers, according to the petrographic characteristics, grain size parameters and
element geochemistry, were identified. Meanwhile, indicators including total
sulfur (TS)/total organic carbon (TOC) ratio, $CaCO_3$ content, and chromium-
reducible sulfur (CRS) revealed these horizons were mostly related to methane
seep events. Constrained by foraminifera shells AMS[14]C results, these events
were determined to have occurred from the LGM to early Holocene, Similar
records in the northern and southern slopes suggests the universal occurrence
of these small-scale layers in the SCS. The comprehensive analysis showed that
the development of these event layers over the past 25 ka can be divided into
three stages, 25-15.5 ka, 15.5-7 ka and 7 ka to present. Late Quaternary Ocean
environment changes, especially sea level and bottom water temperature,
controlled the occurrence of regional small-scale event layers in the SCS. The
regional scale mechanism is that the pressure and temperature change affect the
stability of hydrate and the methane seepage, and thus the strata stability.
Corresponding to the lowest, the rapid increase and the highest levels of the
sea level and bottom water temperature, the temporal evolution pattern of
small-scale event layers in the SCS showed a highest, decreased and lowest

frequency, respectively. The linkage between the late Quaternary marine environmental change and turbidite deposition through gas activities in this study can act as a useful reference for further understanding the continental margin sedimentary process.

1 Introduction

The continental margin experiences active sedimentation and is a transit station for the transportation of materials from land to deep ocean. As a geomorphic unit connecting the shallow continental shelf and deep ocean basin, the continental slope contains various sedimentary types, e.g. hemipelagic, gravity-flow, and contourite depositions. The turbidity current, a gravity flow composed of sediment and water with a density greater than that of the surrounding water, is a characteristic geological agent of sediment transport and deposition in the slope Sedimentologists have struggled to decipher the environmental signals contained in the strata due to the unsteady environment resulting from frequent turbidity currents. Therefore, extracting information for the continuous evolution of the geological environment from instantaneously triggered deep-sea turbidite deposition is an challenge in deep-sea sedimentology (Zaragosi et al., 2006; Toucanne et al., 2008; Pouderoux et al., 2012; Lombo Tombo et al., 2015; Yu et al., 2017; Li et al., 2021a). The occurrence of deep-sea turbidity currents is closely related to strata collapse, which presents hidden dangers to engineering safety. Large-scale strata collapse can result in the formation of a tsunami (Nisbet and Piper, 1998), thereby posing danger to residents. In addition, the coarse-grained sedimentary strata formed under the turbidite environment are good reservoirs of deep-sea oil and gas hydrate, which is of great significance for the exploration of deep-sea resources (Rothwell et al., 1998; Mienert et al., 2005; Liang et al., 2017; Liu et al., 2020).

The area around the South China Sea (SCS) contains developed river systems draining basins with active erosion. In the northern SCS margin, currents include different layers of western boundary currents (Wang et al., 2011; Zhou et al., 2017; Zhu et al., 2019), Guangdong Coastal Current and the SCS Warm Current (Guan and Fang, 2006). Additionaly, frequent typhoons and strong internal waves (Alford et al., 2015; Zhang et al., 2018a) combined with the supply of a large number of terrigenous materials lead to frequent turbidity currents on the northern slope of the SCS. Many turbidite layers have been identified in the core samples of the SCS continental slope area in recent decades using geophysics, sedimentology, geochemistry, and mineralogy proxies (Zhao et al., 2011; Jiang et al., 2014; Yu et al., 2017; Li et al., 2019; Liu et al., 2020). This revealed that turbidites with a water depth of 1,000–4,500 m from the slope to the basin have been widely distributed since the last glacial period. Most previous studies focused on medium- to large-scale turbidity activities, with discussion on large-scale collapse or enormous terrestrial materials input. In contrast, there have been relatively few studies on records of small -scale pulsed turbidite events contained in core samples. On the other hand, the proposed complex and diverse turbidity current triggering mechanisms have remained controversial, and include typhoons, earthquakes, floods, etc (Lombo Tombo et al., 2015; Zhang et al., 2018a; Maloney et al., 2020). Proposed mechanisms regulating long term turbidity currents include tectonic activity, sea-level fluctuation, and climate related periodic high sediment supply pulse (Maslin et al., 1998; Ducassou et al., 2009; Lombo Tombo et al., 2015). The hydrate dissociation is a characteristic geological agent in the continental slope that has attracted extensive attention in recent years. Methane leakage can induce collapse and disastrous turbidity current over large scales (Paull et al., 1991; Nisbet and Piper, 1998). For example, the extremely thick turbidite layer of the Mediterranean is related to strata instability induced by methane leakage generated by hydrate decomposition (Rothwell et al., 1998). The enormous collapse of the Norwegian continental margin is also related to the reduction of gas hydrate stability (Mienert et al., 2005; Crémière et al., 2016), and even triggered a tsunami (Bondevik et al., 2005). The SCS is one of the most important gas hydrate reservoirs. Bottom simulating reflectors, mud volcanoes, mud diapirs and gas chimneys have all been found in ashes associated with natural gas hydrates. In addition, due to the unstable state of hydrate, methane seepage is common in the SCS slope. Recent studies showed widespread methane leakage in the SCS slope. However, most leaks are of a small scale and weak intensity. No catastrophic collapse resulting from large-scale leakage is contained in geological records. Therefore, various uncertainties remain, including: (1) How could we identify the deep-sea turbidite layers in the SCS precisely; (2) whether such the small-scale coarse-grained event layers commonly existing in the SCS slope are related to methane leakage activities; (3) the role of marine environmental change during the late Quaternary in formation of these small-scale event layers. The present study selected a gravity core from the "Haima" seep area in the northwestern SCS, comprehensively compared with the records of other cores taken from the southern and northern slopes of the SCS to discuss the possible relationship between turbidite records and methane leakage and control mechanism in the SCS since the LGM.

2 Materials and methods

2.1 Materials

The core Q6 (water depth: 1,400 m; length: 2.72 m) used in the present study was collected by the Guangzhou Marine Geological Survey using the Haiyang-6 vessel between April and May, 2019 (Figure 1). The core site is on the north western continental slope of the SCS. In general, the core shows relatively homogeneous silty-clay deposition, besides for three obviously coarsened sand layers (Figure 2). The potential pulsed turbidite layers of the core were identified using petrography, sedimentology, and geochemistry proxies. The layers significantly affected by methane leakage were identified using geochemistry proxies. Eight layers were chosen for AMS[14]C ages measurements (Figure 2) using planktonic foraminifera *Globorotilia menardii* shells in BETA laboratory (U.S.), and the results has been reported in our previous work (Miao et al., 2021a).

2.2 Grain-size analyses

Solutions of 15 mL 30% H_2O_2 and 5 mL 3 mol/L HCl were added to remove organic matter and carbonate. All samples were fully desalted and dispersed before measurements. The samples were analyzed using a Mastersizer 2000 instrument (range: 0.02–2,000 μm; resolution: 0.01Φ) at the Key Laboratory of Submarine Geosciences and Prospecting, Ministry of Education, China. The error based on repeated measurements was estimated to be less than 3%.

2.3 Geochemical element analyses

Prior to the analyses, 0.05 g freeze-dried sample was dissolved twice in HF-HNO$_3$ (1:1) and dried again at 190°C for 48 h. Approximately ~50 g of the mixture was then prepared and
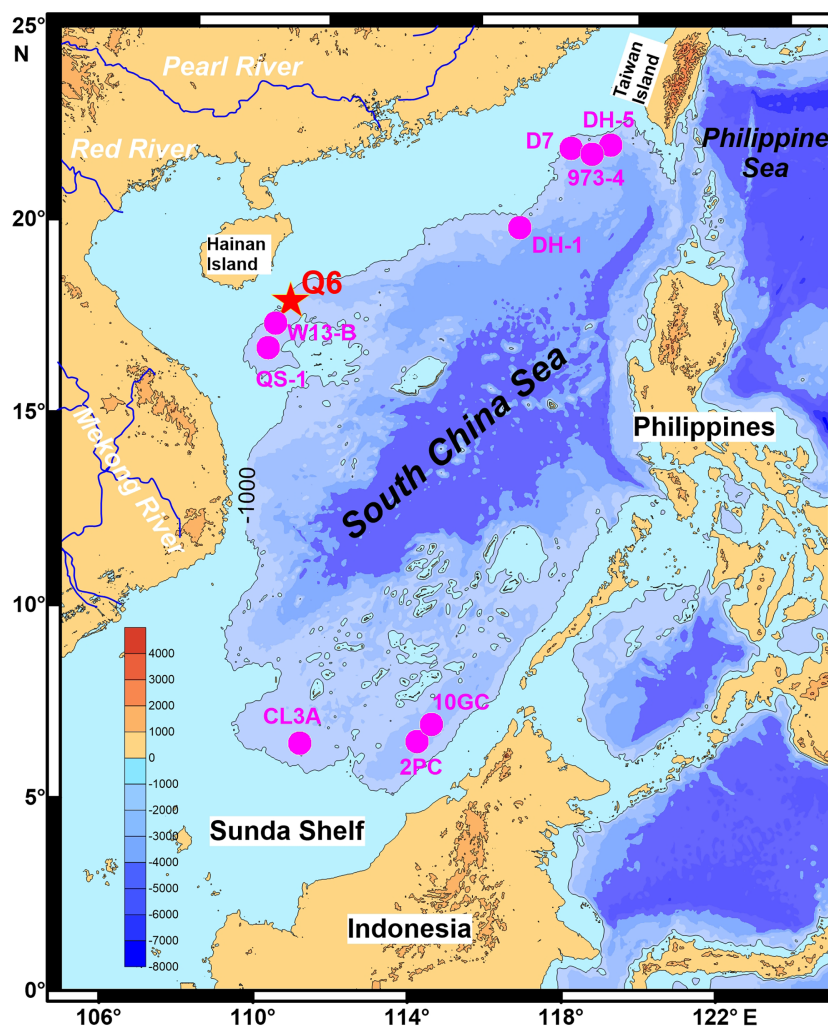
FIGURE 1
Map showing the study area in the SCS. The red star indicates the sampling location of Q6 and the magenta cycles indicate referenced cores in this study.

FIGURE 2
Photographs and lithological description of the core Q6.
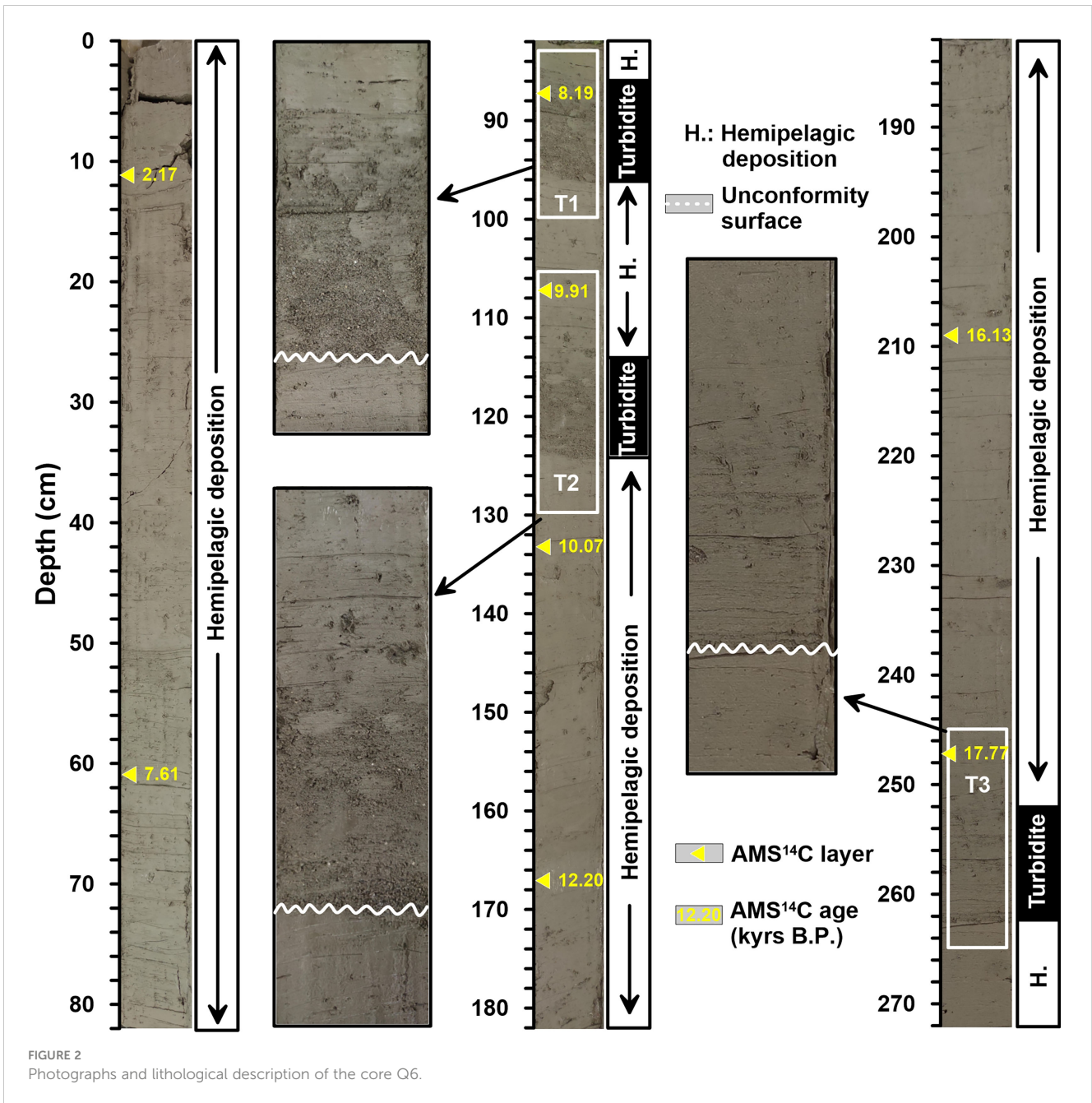
measured. Nearly 10% of these samples were analyzed in replicates to determine the measurement error, and the elemental compositions of a GSD-9 reference standard were measured to confirm the accuracy of the analyses. The geochemical element analysis, including the measurement of major and trace elements was conducted by the Experiment-Testing Center of Marine Geology, Ministry of Land and Resources. The major elements in the sediments were analyzed using inductively coupled plasma atomic emission spectroscopy (ICP-AES), and the standard deviation of these measurements was < 1%. The trace elements in the sediments were analyzed by ICP mass spectrometry (ICP-MS), and the standard deviation of these measurements was < 5%.

2.4 Total organic carbon analyses

Accurately weigh about 1g of freeze-dried sediment and ground to 200 mesh. Approximately 2 mL of 1 mol/L HCl was then added, and the sample was soaked and submitted to ultrasound to remove inorganic carbon. The sample was then placed on a low-temperature electric heating plate for 12 h to volatilize HCl. After drying, 50 mg of sediment was placed in an elemental analyzer (Elementar Vario ELIII, Germany) and organic carbon (TOC) was determined in the CN mode. The sediment was dried under low temperature, after which 50 mg was extracted and placed directly on the elemental analyzer for the determination of total carbon (TC). A

standard sample GSD-9 and 10% parallel sample were analyzed concurrently during the test. The standard deviations of TC and TOC were 0.004% and 0.006%, respectively. The measurement was completed in the Key Laboratory of Marine Geology and Metallogeny, First Institute of Oceanography, Ministry of Natural Resources. $CaCO_3$ content was calculated as:

$$CaCO_3(\%) = (TC - TOC) \times 8.33 \qquad (1)$$

2.5 Chromium reducible sulfur analyses

Chromium-reducible sulfur (CRS) was analyzed according to the method described by Canfield et al. (1986). The bulk sediments were dried and grounded to homogeneous powders of 200 mesh size. Then, pyrite extraction was carried out by weighing 50–200 mg samples. CRS was reduced using 1.0 M $CrCl_2$-0.5 M HCl and 3N HCl solutions under a continuous flow of nitrogen for 2 h at 200–250°C. The liberated H_2S was trapped in an $AgNO_3$-NH_4OH solution and converted into Ag_2S precipitates. The percentage of pyrite could be calculated by the amount of Ag_2S extracted.

3 Results and discussion

3.1 Identification of turbidite layers

The turbidite layer often produces obvious unconformity in comparison with stable and continuous hemipelagic sediments. This is due to the significant scouring of the underlying strata by the high concentration of suspended sediment, resulting in significant variation in grain size (including higher sand content, coarser mean grain size or median grain size, and a finer positive sequence from bottom to top), higher coarse-grained detrital minerals, such as quartz and zircon, and higher Si/Al, Si/Fe, and Zr/Rb ratios (Fournier et al., 2016; Fauquembergue et al., 2019; Di et al., 2021; Liu et al., 2021; Li et al., 2021a). Core Q6 contains three layers with obvious coarsening grain size at 88–96 cm, 116–128 cm, and 254–260 cm, respectively. These layers are in obvious unconforming contact with the underlying strata, of which the sand particles in the 88–96 cm and 116–128 cm layers are clearly visible by the naked eye (Figure 2). The characteristic grain size end-members were extracted using the inversion model (Dobigeon et al., 2009; Schmidt et al., 2010; Joussain et al., 2016) (Figure 3) to further identify the possible small-scale pulsed turbidite layers not visible by the naked eye and to limit the dynamic changes of the deposition process. The first three fractions explained ~96.3% of all variations, and covered almost all the core data. Therefore, three end-members were chosen to explain data variation. End-member 1 (EM 1) varied between 1 μm–30 μm, with a peak of 5 μm; End-member 2 (EM 2) varied between 1 μm–40 μm, with a peak of 6 μm; End-member 3 (EM 3) showed the widest range of between 1 μm–300 μm, with a peak of 30 μm. EM 3 showed similar trends with sand fraction content and median grain size (Figure 4). Therefore, this end member was the key to regulating variations in grain size. EM 3 also showed several obvious pulse peaks, which were a good

indication of the above three potential turbidite layers and in good agreement with the local peak records of Si/Al, Si/Fe and Zr/Rb ratios. Based on the above evidence, eight possible turbidite layers were identified: 88–96 cm, 116–128 cm, 140–148 cm, 160–162 cm, 212–214 cm, 230 cm, 238–240 cm, and 254–260 cm. Particle size distribution curves for these layers show obvious bimodal distribution with an additional coarse-grained peak than the hemipelagic layers (Figure 3). The C-M diagram based on the sediment cumulative frequencies of 1% (coarsest component) and 50% (median grain size) contents were used to assess the dynamic deposition environment through different sediment transport dynamics (Passega, 1957; Passega, 1977). Here, turbidite deposition was parallel to the C=M line. The C-M diagram of these eight potential turbidite layers was used to determine that the distributions of the 88–96 cm, 116–128 cm, and 254–260 cm layers were roughly parallel to the C=M line (Figure 5A), which is a typical turbidite deposition feature. In contrast, the distributions of the 140–148 cm, 160–162 cm, 212–214 cm, 230 cm, and 238–240 cm layers were roughly parallel to the horizontal axis (Figure 5B). Since these distributions were consistent with the distribution characteristics of other hemipelagic layers (Figure 5C), the genesis could not yet be determined. Some layers may contain coarser particles in a limited range due to hydrodynamic factors such as bottom current enhancement. Alternatively, some layers may show small-scale turbidite deposition resulting from gas hydrate dissociation environment (to be analyzed below). The samples did not show typical turbidite characteristics due to their small number. It should be noted that there was no clear positive grain sequence structure of turbidite layers, which may be transformed by later hydrodynamic forces. The hydrodynamics of the northern slope of the SCS is complex and includes a highly active contour current activity (Chen et al., 2014; Zhao et al., 2015). The northwestern slope encounters the anticyclonic intermediate water circulation of the SCS (Chen et al., 2014), which is likely to transform the existing sediments. However, no obvious sedimentological evidence exists at present, calling for the need for further analyzes in combination with more data. Although the geochemical indices of the 212–214 cm and 230 cm layers were high, there was no indication of EM 3 (Figure 4). This result could possibly be attributed by the increase in the content of authigenic minerals, such as opal.

3.2 Identification of methane seep events

The sediments of the methane seep environment usually show abnormal enrichment of authigenic carbonate and pyrite due to the existence of sulfate-driven anaerobic oxidation of methane (SD-AOM) (Jørgensen et al., 2004; Peckmann et al., 2004; Bayon et al., 2007; Bayon et al., 2013; Han et al., 2014; Crémière et al., 2016; Lin et al., 2016; Liu et al., 2020). This eventually leads to clear changes in sediment geochemical characteristics, such as the CRS, TS/TOC ratio and $CaCO_3$ (Peketi et al., 2012; Sato et al., 2012; Li et al., 2018; Miao et al., 2021a; Miao et al., 2021b; Miao et al., 2022). Under a normal environment without methane seepage, labile organic matter is gradually degraded by sulfate-reducing bacteria *via* organoclastic sulfate reduction (OSR) and this biogeochemical
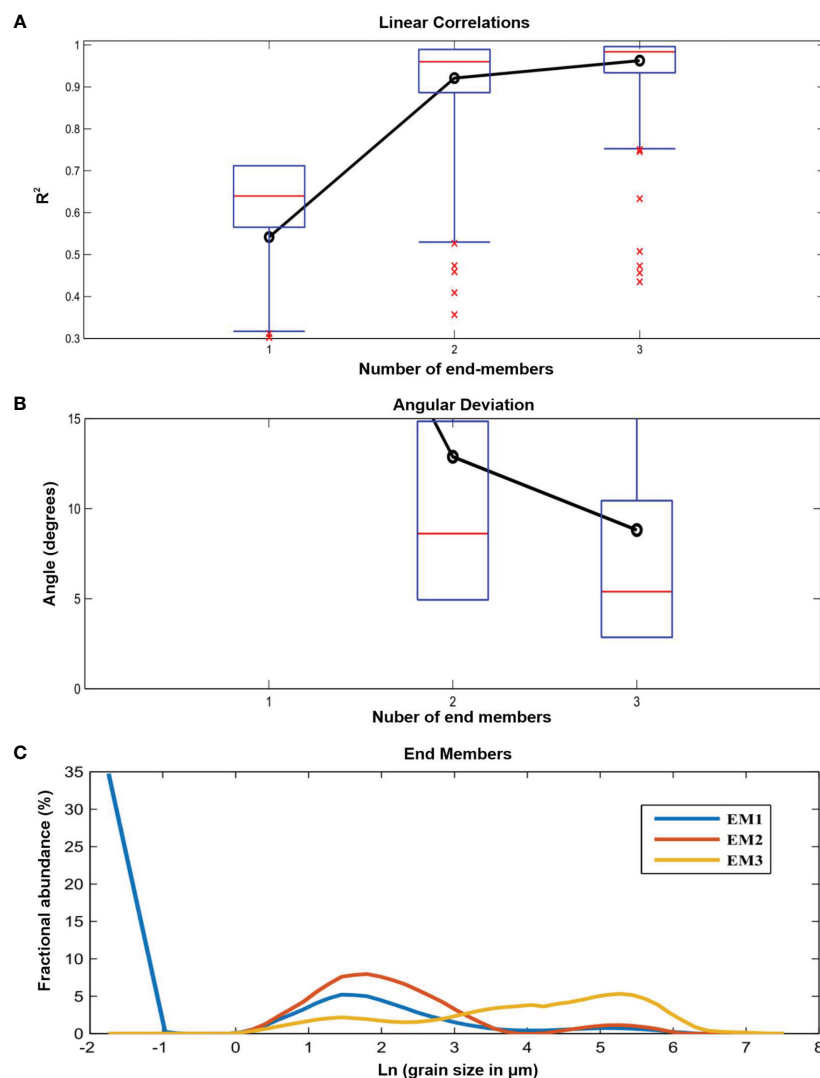
FIGURE 3
(A) Fraction of data variance explained by the unmixing model vs. number of end-members. **(B)** Volume percent vs. grain size (µm) diagram of the three end- members (EM1, EM2, and EM3) identified in core Q6 **(C)**.

process would produce H$_2$S (Jørgensen, 1982; Lim et al., 2011). Hydrogen sulfide eventually mixes with iron ions in the environment to form pyrite (Jørgensen, 1982). At this time, there is a significant positive correlation between TS and TOC, and the ratio of TS/TOC fluctuates between 0.1 and 0.5 (average of ~0.36) (Berner, 1982; Wei and Algeo, 2020). However, SD-AOM resulting from the methane seep provides a large quantity of additional hydrogen sulfide for the pyrite formation process, promotes the enrichment of authigenic pyrite in the methane anaerobic oxidation zone (SMTZ), and leads to an increase in the CRS content and TS/TOC ratio (Boetius et al., 2000; Peketi et al., 2012). In addition, the additional H$_2$S input destroys the positive relationship between TOC and TS (Sato et al., 2012; Li et al., 2018; Miao et al., 2021b).The TS/TOC ratio in the core Q6 mostly exceeded 0.36 and the organic matter content was low (generally < 1.4%), inconsistent with the sulfate reduction of organic debris. In particular, the TS/TOC ratios of layers 88–96 cm, 116–128 cm, 160–162 cm, 212–214 cm, 230 cm, 238–240 cm, and 254-260 cm increased significantly, and were

generally all above 0.5. The exceptions were those of layers 88–96 cm, 116–128 cm, 160–162 cm, and 254–260 cm, which were > 1.0 (Figures 6B, D). Furthermore, we further analyzed the correlation between TOC and TS and CRS (Figure 7). We found a significant positive between CRS and TS (R^2 = 0.94), indicating that TS mainly consists of pyrite and other inorganic sulfur. At the same time, CRS and TS have no significant correlation with TOC (R^2 = 0.13 and R^2 = 0.04, respectively), which indicates that pyrite generation has little relationship with TOC. Moreover, SD-AOM-pyrite usually has a heavy sulfur isotope value, which is also considered to be an important marker for identifying methane seepage activities (Jørgensen et al., 2004; Lin et al., 2016). In the previous work, we also found the phenomenon of increasing sulfur isotope value of pyrite in these horizons (Miao et al., 2021b). Therefore, this result showed that pyrite is obviously enriched in these layers in the core Q6 and is affected by SD-AOM (Figures 6B, G–I). In addition, SD-AOM also makes the environment more alkaline and produces large amounts of carbonates (Peckmann et al., 2004; Bayon et al.,
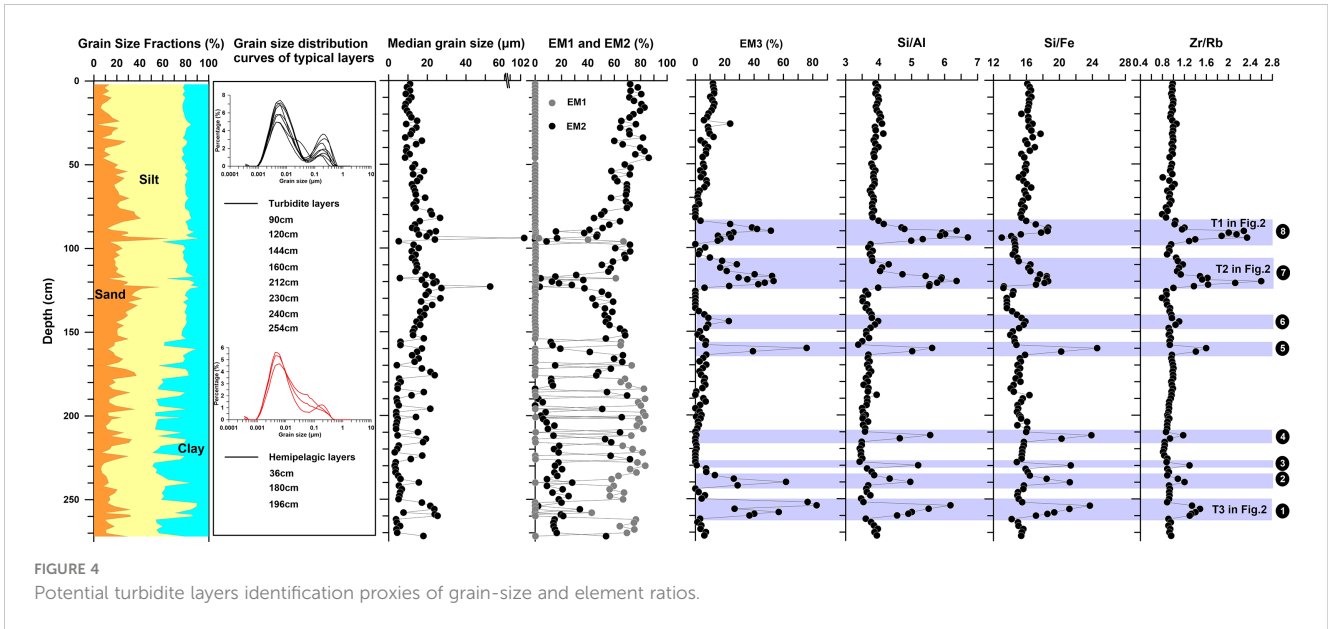
FIGURE 4

Potential turbidite layers identification proxies of grain-size and element ratios.

2007; Bayon et al., 2013). In Q6, it is found that CaCO₃ content also increases in pyrite enriched horizons. The CaCO₃ content was significantly higher than that of other hemi-pelagic layers. Similar phenomena have been observed in other hydrate areas, such as the Bay of Bengal (Peketi et al., 2012) and the Beikang Basin (Li et al., 2018). Therefore, we can believe that the above layers are obviously affected by methane seep.

3.3 Pulsed turbidite and methane seep events: Sea-level and bottom temperature forcing

The factors that induce strata instability and result in turbidity current include occasional earthquakes, typhoons, volcanic activity, instantaneous pulse of high sediment supply, sea level fluctuation, gas hydrate decomposition, and leakage (Masson, 1996; Maslin et al., 1998; Prins and Postma, 2000; Ducassou et al., 2009; Lombo Tombo et al., 2015; Crémière et al., 2016; Zhang et al., 2018b; Maloney et al., 2020; Li et al., 2021a). The instantaneous pulse of

high sediment supply is generally related to a sharp increase in the quantity of erosion material. This is regulated by regional climate conditions or the rapid entry of a large quantity of sediment into the ocean caused by flood events (Ducassou et al., 2009). Lower precipitation occurred both in the the East Asian summer monsoon and Indian summer monsoon regimes during the LGM period, whereas pulsed turbidite events occurred frequently in many regions of the SCS (Hu et al., 2017; Li et al., 2017; Liu et al., 2020; Di et al., 2021; Feng et al., 2021; Li et al., 2021b). Clearly, these observations cannot be explained by strata instability caused by the increase in the instantaneous sediment supply in the source area alone. There has been no record of such high-frequency volcanic eruptions around the SCS since the LGM. Sea level fluctuation regulates the accumulation of sediment and controls the strata pressure by changing the accommodation space, which may affect the hydrate dissociation and induce strata instability. Examples include the Amazon fan, the southern Carolina rise, and the inner Blake Ridge, etc (Paull et al., 1996; Maslin et al., 1998). As instantaneous triggering factors, occasional earthquakes and typhoons are difficult to identify at a geological scale and may
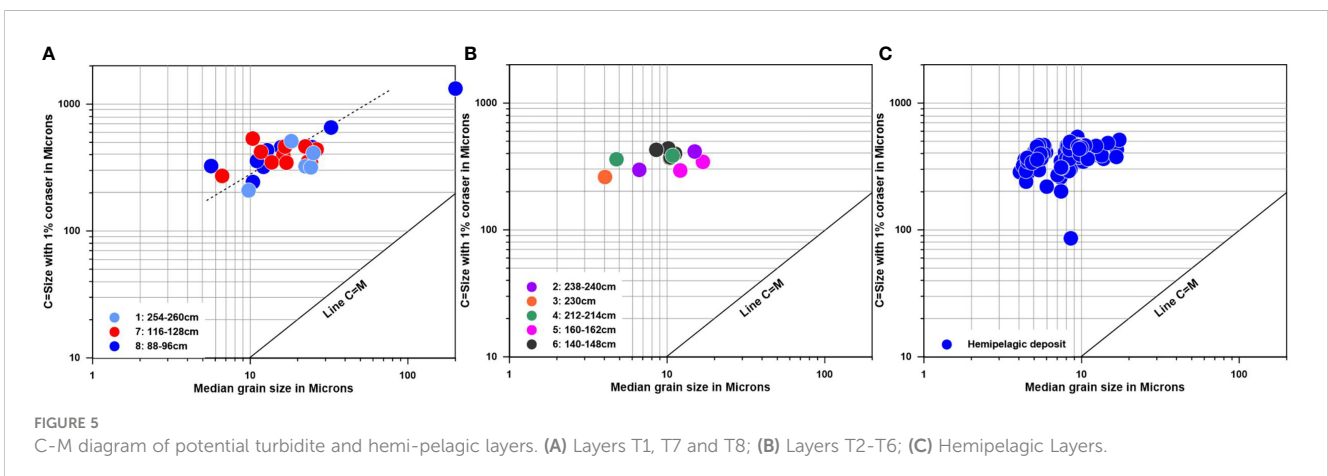
FIGURE 5

C-M diagram of potential turbidite and hemi-pelagic layers. **(A)** Layers T1, T7 and T8; **(B)** Layers T2-T6; **(C)** Hemipelagic Layers.

FIGURE 6
Identification proxies for methane release layers. **(A)** Si/Al; **(B)** CaCO$_3$(%); **(C)** CRS (wt.%); **(D)** TS/TOC; **(E)** Si/Al between 200-250cm; **(F)** TS/TOC between 200-250cm; **(G–I)** Scanning electron microscopy (SEM) pictures of pyrite aggregates in samples. TS/TOC and SEM pictures according to Miao et al. (2021b).
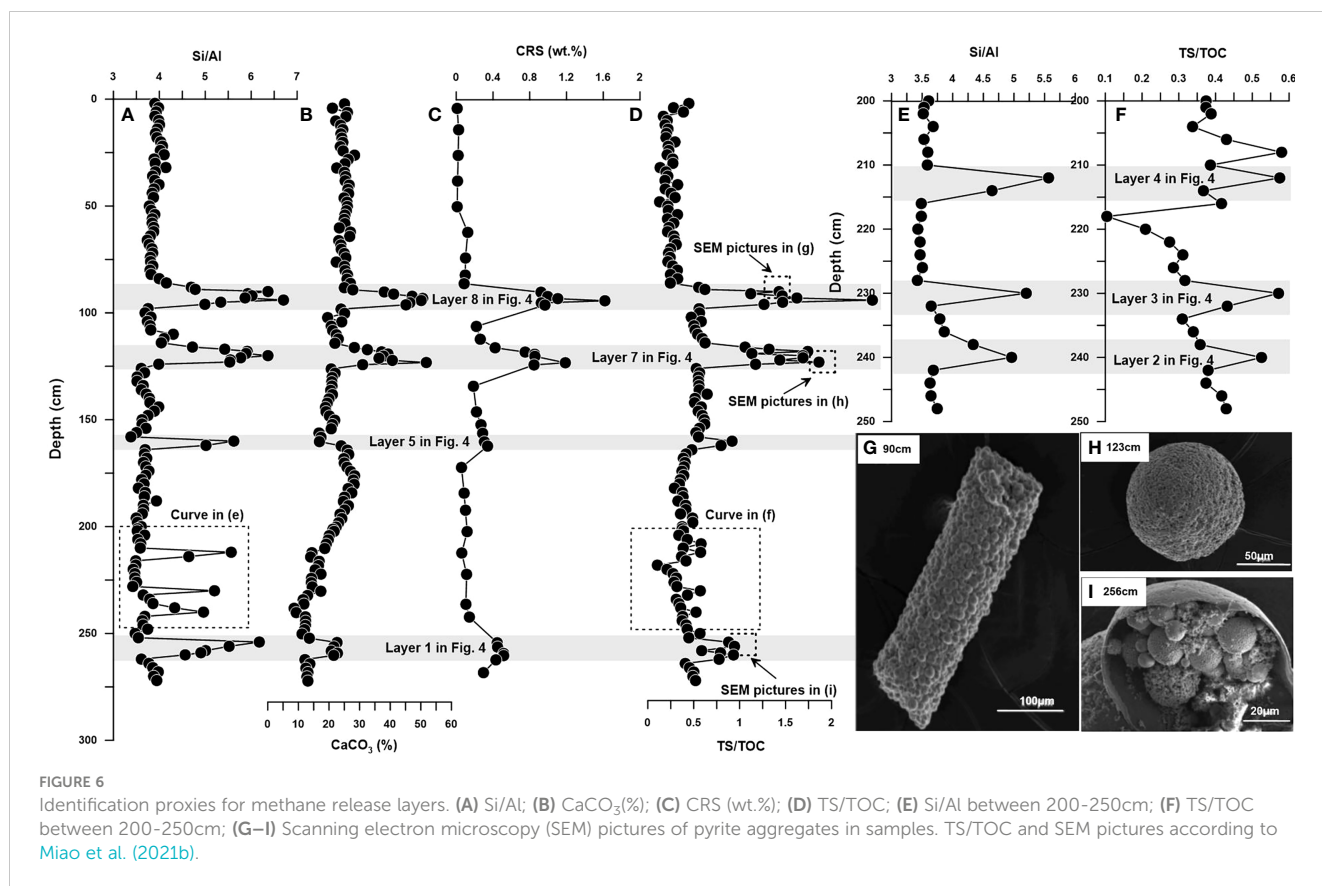
need to be comprehensively analyzed in combination with other factors.

Gas hydrate dissociation is common in the continental slope area and is generally considered to occur due to changes in temperature and pressure (Phrampus and Hornbach, 2012; Tong et al., 2013; Crémière et al., 2016). A low temperature and high-pressure environment are suitable for hydrate storage, whereas the opposite is conducive to hydrate dissociation. The sea level and bottom water temperature of the SCS have increased significantly since the LGM (Shackleton, 1987; Fairbanks, 1989; Waelbroecka et al., 2002; Lisiecki and Raymo, 2005; Bates et al., 2014; Wan and Jian, 2014) (Figure 8). Therefore, the changes in pressure and temperature during this process can play a key role in the hydrate

dissociation. The present study integrated the hydrate dissociation records of several cores in the northwestern slope, northeastern slope, central northern slope, and southern slope areas of the SCS (Figure 8). The results showed that the dissociation of hydrate could be roughly divided into three stages according to the characteristics of sea level and bottom water temperature: (1) 25–15.5 ka, characterized by a low sea level (low pressure) and low temperature stage during which methane leakage was common; (2) 15.5–7 ka, characterized by rising trends in sea level and temperature and in which methane leakage activity was common and continuous, although this activity stopped during the latter part of this stage; (3) 7 ka to the present, characterized by a low activity of methane leakage at a high sea level (high pressure) and high

FIGURE 7
CRS-TS-TOC diagram. **(A)** CRS *vs* TS; **(B)** CRS *vs* TOC; **(C)** TS *vs* TOC.
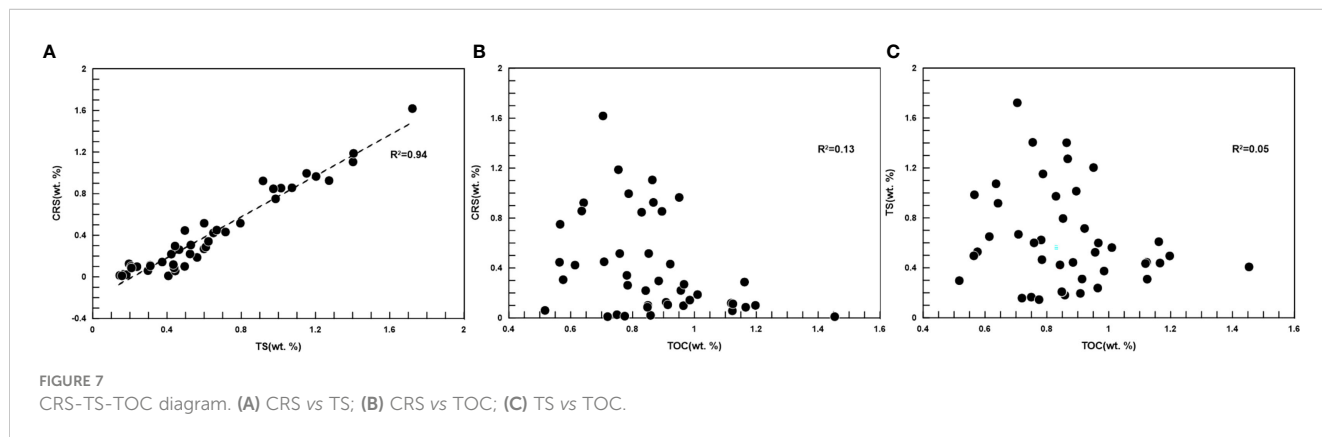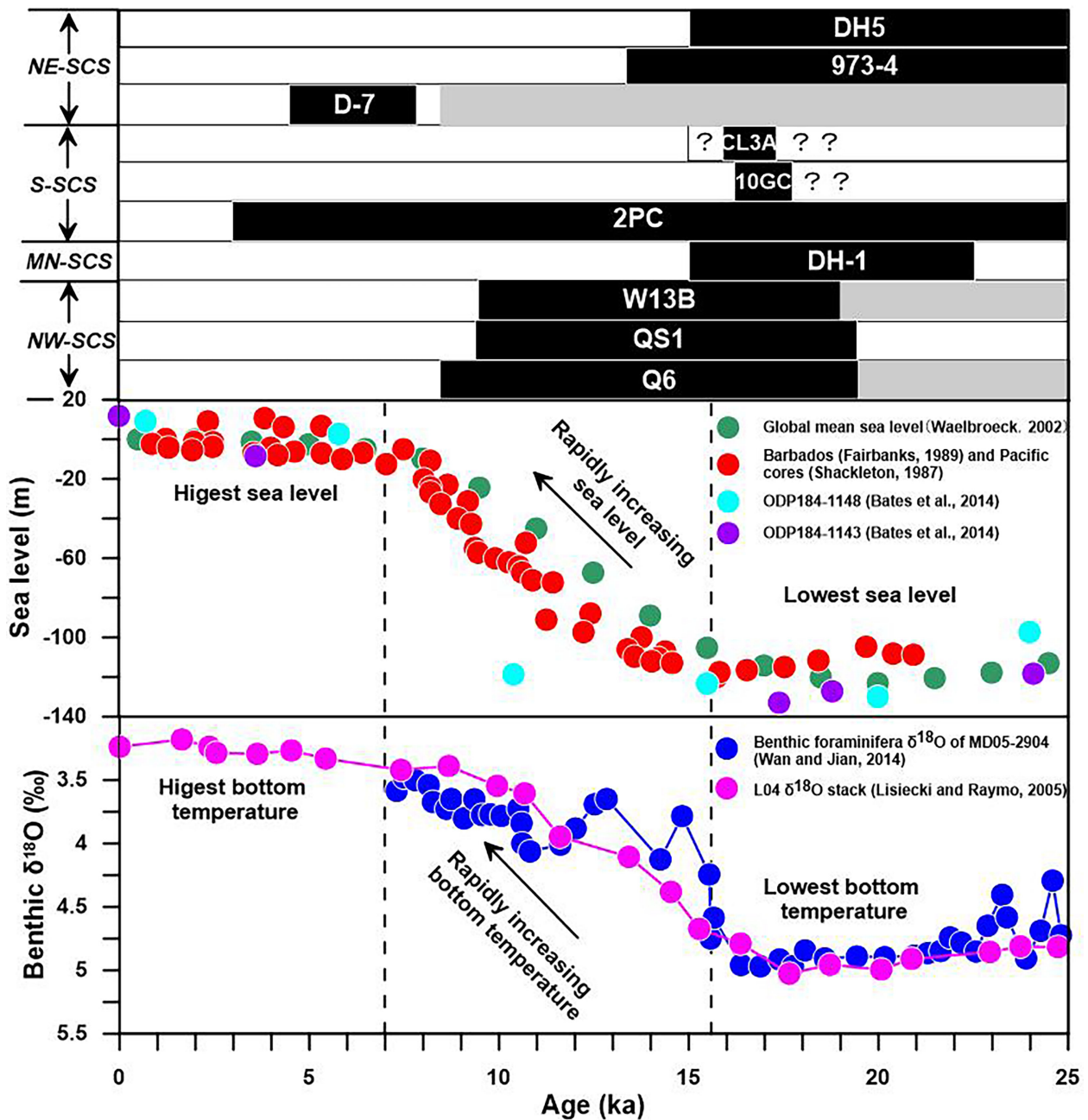
FIGURE 8

Comparison of methane leakage records in the South China Sea and reconstruction results of sea level and bottom water temperature. NE-SCS, northeastern South China Sea; S-SCS, southern South China Sea; MN-SCS, middle-northern South China Sea; NW-SCS, northwestern South China Sea. The black, grey and white rectangular bars show time ranges of methane release events, data absence and normal hemipelagic layers with no methane release events, respectively. The interrogation mark show records with no accurate age points. Data sources: DH5, W13B and 2PC (Li et al., 2021b); CL3A (Feng et al., 2021); DH-1 (Li et al., 2017); D-7 (Hu et al., 2017); QS1 (Liu et al., 2020); 10GC (Di et al., 2021); 973-4 (Zhang et al., 2018b); Q6 (This study). Sea-level reconstruction results are from global mean (Waelbroecka et al., 2002), Barbados (Fairbanks, 1989), Pacific cores (Shackleton, 1987), ODP184-1143 and ODP184-1143 (Bates et al., 2014). Bottom temperature results: Benthic foraminifera δ^{18}O of core MD05-2904 (Wan and Jian, 2014) and the LR04 stack (Lisiecki and Raymo, 2005).

temperature. The effects of sea level and bottom water temperature on gas hydrate were opposite in each stage.

The sea level dropped by over 100 m during the regression of the late Pleistocene, resulting in a decrease in the pressure on the seabed by 1,000 kPa (Wang et al., 2004). The reduction in total pressure resulted in the dissociation of natural gas hydrate, the release of large quantities of methane and water, and an increase in

slope instability. These changes occurred globally, and resulted in nearly 200 landslides on the continental margin of the Atlantic in the United States, the continental slope of Southwest Africa, the continental margin of Norway, the continental margins of the Beaufort Sea, the Caspian Sea, the north Panama continental shelf and Newfoundland. The Amazon submarine landslide is attributed to the rapid decline in sea level. This is because the drop in sea level

induced an instability in natural gas hydrate and to the sliding of overlying sediments (Maslin et al., 1998). The sea level decreased significantly during the last glacial period, particularly in the LGM, during which the sea level was 120 m below the current level in the SCS. The strata pressure overlying the gas hydrate decreased significantly, inducing dissociation leakage, which was recorded widely in slope areas of the SCS (Hu et al., 2017; Li et al., 2017; Zhang et al., 2018b; Liu et al., 2020; Di et al., 2021; Feng et al., 2021; Li et al., 2021b) (Figure 8). Although the low temperature during this period was suitable for maintaining the stability of hydrate, the significant reduction in pressure dominated the release of gas hydrate. The factors triggering strata instability may include an occasional earthquake, typhoon, or flood. For example, observations of a submarine canyon in the northern SCS confirmed that typhoon triggered turbidity currents (Zhang et al., 2018a). At the initiation of a landslide, free gas under the hydrate layer rises along the crack, and the hydrate in the original metastable state will decompose and release methane gas. This release of gas will have a significant impact on the seabed redox environment, such as deep-water oxygen consumption (Bayon et al., 2013) and seawater sulfate concentration (Crémière et al., 2013; Kiel, 2015). These processes explain the significant increases in CRS, TS/TOC, CaCO$_3$ and pyrite (Figure 6).

There were rapid increases in the sea level and bottom water temperature between 15.5–7 ka. Gas hydrate leakage records continued to be recorded in almost all areas, and significantly decreased or stagnated during this period (Figure 8). This result indicated that leakage activity continued concurrent with the significant pressurization and heating of the storage environment. Leakage activity then almost stagnated under pressure after a period. The rapid rise in bottom water temperature since 15.5 ka likely promoted the dissociation of gas hydrate, offset the inhibition of hydrate dissociation resulting from sea-level rise-induced pressure increase to a certain extent, and maintained the occurrence of methane leakage until the early Holocene. This mechanism is similar to the hydrate dissociation and release of a large quantity of methane gas from many continental margins globally during the Quaternary glacial-interglacial transition period, which is often attributed to the rise of bottom water temperature (Dean et al., 2015; Himmler et al., 2019; Kennett James et al., 2000; Reagan and Moridis, 2007). Hydrate decomposition events have been identified in the transition periods of MIS10/9 (Tong et al., 2013)、 MIS6/5(Chen et al., 2019; Deng et al., 2021)、 MIS4/3 (Han et al., 2014; Yang et al., 2018)、 MIS2/1(Feng and Chen, 2015; Wei et al., 2020; Deng et al., 2021) in the SCS. These events indicate that the significant change in temperature was indeed conducive to hydrate dissociation. Although there was no obvious change in bottom water temperature since the early Holocene, the sea level continued to rise rapidly. The increasing overlying sea water pressure maintained the stable state of hydrate. Hydrate begins to form in large quantities once the appropriate conditions are met and dissociation is halted.

The highest sea level and bottom water temperature have occurred since 7 ka, and the records indicate significant decreases in gas hydrate dissociation in various regions of the SCS (Figure 8). Although modern seafloor observations show continued methane gas leakage (Zhang et al., 2020), the stratigraphic records show no turbidite layer formed by strata instability resulting from methane leakage.

4 Conclusions

According to multi-disciplinary indicators, the small-scale deep-sea turbidite and methane seep event layers in a gravity core in the northwestern SCS were identified, and the role of the changes in the sea level and paleoceanography environment during the late Quaternary in the formation of the above layers was discussed, and the following understanding was formed:

(1) Based on the petrographic characteristics, grain size parameters and element geochemistry indicators, eight potential pulsed turbidite layers were identified. Meanwhile, indicators including TS/TOC ratio, CaCO$_3$ content, and CRS revealed these horizons were mostly related to methane seep events.

(2) These event layers mainly occurred from the LGM to early Holocene, when low sea level and transgression were universal to the SCS continental slope, indicating a high incidence of small-scale turbidite layers and methane seepage events.

(3) Development of these small-scale pulsed turbidite and methane seep events could be divided into three stages: 25–15.5 ka, 15.5–7 ka and 7 ka. The variations in strata pressure over hydrate resulting from the changes in sea level and bottom water temperature were suggested the main factors regulating methane seepage, which affected strata stability of the continental slope and the occurrence of pulsed turbidite events.

Data availability statement

The original contributions presented in the study are included in the article/Supplementary Material. Further inquiries can be directed to the corresponding author.

Author contributions

JL, XF and JW: Conceived the project, write and correct the manuscript. XM, RJ and MZ: Participated in scientific interpretation and editing. XD and QX: Carried out sample pretreatment and measurements. All the authors contributed to the data interpretation and writing of the paper. All authors contributed to the article and approved the submitted version.

Funding

Acknowledgments

Conflict of interest

The authors declare that the research was conducted in the absence of any commercial or financial relationships that could be construed as a potential conflict of interest.

Publisher's note

All claims expressed in this article are solely those of the authors and do not necessarily represent those of their affiliated organizations, or those of the publisher, the editors and the reviewers. Any product that may be evaluated in this article, or claim that may be made by its manufacturer, is not guaranteed or endorsed by the publisher.

Supplementary material

The Supplementary Material for this article can be found online at: https://www.frontiersin.org/articles/10.3389/fmars.2023.1147751/full#supplementary-material

References

Alford, M. H., Peacock, T., MacKinnon, J. A., Nash, J. D., Buijsman, M. C., Centuroni, L. R., et al. (2015). The formation and fate of internal waves in the south China Sea. *Nature* 521, 65–69. doi: 10.1038/nature14399

Bates, S. L., Siddall, M., and Waelbroeck, C. (2014). Hydrographic variations in deep ocean temperature over the mid-pleistocene transition. *Quaternary Sci. Rev.* 88, 147–158. doi: 10.1016/j.quascirev.2014.01.020

Bayon, G., Dupré, S., Ponzevera, E., Etoubleau, J., Chéron, S., Pierre, C., et al. (2013). Formation of carbonate chimneys in the Mediterranean Sea linked to deep-water oxygen depletion. *Nat. Geosci.* 6, 755–760. doi: 10.1038/ngeo1888

Bayon, G., Pierre, C., Etoubleau, J., Voisset, M., Cauquil, E., Marsset, T., et al. (2007). Sr/Ca and Mg/Ca ratios in Niger delta sediments: Implications for authigenic carbonate genesis in cold seep environments. *Mar. Geol.* 241, 93–109. doi: 10.1016/j.margeo.2007.03.007

Berner, R. A. (1982). Burial of organic carbon and pyrite sulfur in the modern ocean; its geochemical and environmental significance. *Am. J. Sci.* 282, 451. doi: 10.2475/ajs.282.4.451

Boetius, A., Ravenschlag, K., Schubert, C. J., Rickert, D., Widdel, F., Gieseke, A., et al. (2000). A marine microbial consortium apparently mediating anaerobic oxidation of methane. *Nature* 407, 623–626. doi: 10.1038/35036572

Bondevik, S., Mangerud, J., Dawson, S., Dawson, A., and Lohne, Ø. (2005). Evidence for three north Sea tsunamis at the Shetland islands between 8000 and 1500 years ago. *Quaternary Sci. Rev.* 24, 1757–1775. doi: 10.1016/j.quascirev.2004.10.018

Canfield, D. E., Raiswell, R., Westrich, J. T., Reaves, C. M., and Berner, R. A. (1986). The use of chromium reduction in the analysis of reduced inorganic sulfur in sediments and shales. *Chem. Geol.* 54, 149–155. doi: 10.1016/0009-2541(86)90078-1

Chen, F., Wang, X., Li, N., Cao, J., Bayon, G., Peckmann, J., et al. (2019). Gas hydrate dissociation during Sea-level highstand inferred from U/Th dating of seep carbonate from the south China Sea. *Geophys. Res. Lett.* 46, 13928–13938. doi: 10.1029/2019GL085643

Chen, H., Xie, X., Van Rooij, D., Vandorpe, T., Su, M., and Wang, D. (2014). Depositional characteristics and processes of alongslope currents related to a seamount on the northwestern margin of the Northwest Sub-basin, south China Sea. *Mar. Geol.* 355, 36–53. doi: 10.1016/j.margeo.2014.05.008

Crémière, A., Bayon, G., Ponzevera, E., and Pierre, C. (2013). Paleo-environmental controls on cold seep carbonate authigenesis in the Sea of marmara. *Earth Planetary Sci. Lett.* 376, 200–211. doi: 10.1016/j.epsl.2013.06.029

Crémière, A., Lepland, A., Chand, S., Sahy, D., Condon, D. J., Noble, S. R., et al. (2016). Timescales of methane seepage on the Norwegian margin following collapse of the Scandinavian ice sheet. *Nat. Commun.* 7, 11509. doi: 10.1038/ncomms11509

Dean, W. E., Kennett, J. P., Behl, R. J., Nicholson, C., and Sorlien, C. C. (2015). Abrupt termination of marine isotope stage 16 (Termination VII) at 631.5 ka in Santa Barbara basin, California. *Paleoceanography* 30, 1373–1390. doi: 10.1002/2014PA002756

Deng, Y., Chen, F., Guo, Q., Hu, Y., Chen, D., Yang, S., et al. (2021). Possible links between methane seepages and glacial-interglacial transitions in the south China Sea. *Geophys. Res. Lett.* 48, e2020GL091429. doi: 10.1029/2020GL091429

Di, P., Yang, X., Rashid, H., Zhou, Y., Wang, H., Li, N., et al. (2021). Enhanced sulfidization in a sedimentary turbidite layer from the nansha trough in the southern south China Sea. *Sedimentary Geol.* 421, 105955. doi: 10.1016/j.sedgeo.2021.105955

Dobigeon, N., Moussaoui, Saïd, Tourneret, J., and Carteret, Cédric (2009). Bayesian Separation of spectral sources under non-negativity and full additivity constraints. *Signal Process.* 89, 2657–2669. doi: 10.1016/j.sigpro.2009.05.005

Ducassou, E., Migeon, S., Mulder, T., Murat, A., Capotondi, L., Bernasconi, S. M., et al. (2009). Evolution of the Nile deep-sea turbidite system during the late quaternary: influence of climate change on fan sedimentation. *Sedimentology* 56, 2061–2090. doi: 10.1111/j.1365-3091.2009.01070.x

Fairbanks, R. G. (1989). A 17,000-year glacio-eustatic sea level record: influence of glacial melting rates on the younger dryas event and deep-ocean circulation. *Nature* 342, 637–642. doi: 10.1038/342637a0

Fauquembergue, K., Fournier, L., Zaragosi, S., Bassinot, F., Kissel, C., Malaizé, B., et al. (2019). Factors controlling frequency of turbidites in the Bengal fan during the last 248 kyr cal BP: Clues from a presently inactive channel. *Mar. Geol.* 415, 105965. doi: 10.1016/j.margeo.2019.105965

Feng, D., and Chen, D. (2015). Authigenic carbonates from an active cold seep of the northern south China Sea: New insights into fluid sources and past seepage activity. *Deep Sea Res. Part II: Topical Stud. Oceanogr.* 122, 74–83. doi: 10.1016/j.dsr2.2015.02.003

Feng, J., Li, N., Liang, J., Shang, J., Yang, S., and Wang, H. (2021). Using multi-proxy approach to constrain temporal variations of methane flux in methane-rich sediments of the southern south China Sea. *Mar. Petroleum Geol.* 132, 105152. doi: 10.1016/j.marpetgeo.2021.105152

Fournier, L., Fauquembergue, K., Zaragosi, S., Zorzi, C., Malaizé, B., Bassinot, F., et al. (2016). The Bengal fan: External controls on the Holocene active channel turbidite activity. *Holocene* 27, 900–913. doi: 10.1177/0959683616675938

Guan, B., and Fang, G. (2006). Winter counter-wind currents off the southeastern China coast: A review. *J. Oceanogr.* 62, 1–24. doi: 10.1007/s10872-006-0028-8

Han, X., Suess, E., Liebetrau, V., Eisenhauer, A., and Huang, Y. (2014). Past methane release events and environmental conditions at the upper continental slope of the south China Sea: constraints by seep carbonates. *Int. J. Earth Sci.* 103, 1873–1887. doi: 10.1007/s00531-014-1018-5

Himmler, T., Sahy, D., Martma, T., Bohrmann, G., Plaza-Faverola, A., Bünz, S., et al (2019). A 160,000-year-old history of tectonically controlled methane seepage in the Arctic. *Sci. Adv.* 5, eaaw1450. doi: 10.1126/sciadv.aaw1450

Hu, Y., Chen, L., Feng, D., Liang, Q., Xia, Z., and Chen, D. (2017). Geochemical record of methane seepage in authigenic carbonates and surrounding host sediments: A case study from the south China Sea. *J. Asian Earth Sci.* 138, 51–61. doi: 10.1016/j.jseaes.2017.02.004

Jørgensen, B. B. (1982). Mineralization of organic matter in the sea bed-the role of sulphate reduction. *Nature* 296, 643–645. doi: 10.1038/296643a0

Jørgensen, B. B., Böttcher, M. E., Lüschen, H., Neretin, L. N., and Volkov, I. I. (2004). Anaerobic methane oxidation and a deep H2S sink generate isotopically heavy sulfides in black Sea sediments 1 1Associate editor: D. e. canfield. *Geochimica Cosmochimica Acta* 68, 2095–2118. doi: 10.1016/j.gca.2003.07.017

Jiang, T., Zhang, Y., Tang, S., Zhang, D., Zuo, Q., Lin, W., et al. (2014). CFD simulation on the generation of turbidites in deepwater areas: a case study of turbidity current processes in qiongdongnan basin, northern south China Sea. *Acta Oceanologica Sin.* 33, 127–137. doi: 10.1007/s13131-014-0582-7

Joussain, R., Colin, C., Liu, Z., Meynadier, L., Fournier, L., Fauquembergue, K., et al. (2016). Climatic control of sediment transport from the Himalayas to the proximal NE Bengal fan during the last glacial-interglacial cycle. *Quaternary Sci. Rev.* 148, 1–16. doi: 10.1016/j.quascirev.2016.06.016

Kennett James, P., Cannariato Kevin, G., Hendy Ingrid, L., and Behl Richard, J. (2000). Carbon isotopic evidence for methane hydrate instability during quaternary interstadials. *Science* 288, 128–133. doi: 10.1126/science.288.5463.128

Kiel, S. (2015). Did shifting seawater sulfate concentrations drive the evolution of deep-sea methane-seep ecosystems? *Proc. R. Soc. B: Biol. Sci.* 282, 20142908. doi: 10.1098/rspb.2014.2908

Li, N., Feng, D., Chen, L., Wang, H., and Chen, D. (2017). Compositions of foraminifera-rich turbidite sediments from the shenhu area on the northern slope of the south China Sea: Implication for the presence of deep water bottom currents. *J. Asian Earth Sci.* 138, 148–160. doi: 10.1016/j.jseaes.2017.02.010

Li, M., Ouyang, T., Tian, C., Zhu, Z., Peng, S., Tang, Z., et al. (2019). Sedimentary responses to the East Asian monsoon and sea level variations recorded in the northern south China Sea over the past 36 kyr. *J. Asian Earth Sci.* 171, 213–224. doi: 10.1016/j.jseaes.2018.01.001

Li, J., Shi, X., Liu, S., Qiao, S., Zhang, H., Wu, K., et al. (2021a). Frequency of deep-sea turbidity as an important component of the response of a source-to-sink system to climate: A case study in the eastern middle Bengal fan since 32 ka. *Mar. Geol.* 441, 106603. doi: 10.1016/j.margeo.2021.106603

Li, N., Yang, X., Peckmann, J., Zhou, Y., Wang, H., Chen, D., et al. (2021b). Persistent oxygen depletion of bottom waters caused by methane seepage: Evidence from the south China Sea. *Ore Geol. Rev.* 129, 103949. doi: 10.1016/j.oregeorev.2020.103949

Li, N., Yang, X., Peng, J., Zhou, Q., and Chen, D. (2018). Paleo-cold seep activity in the southern south China Sea: Evidence from the geochemical and geophysical records of sediments. *J. Asian Earth Sci.* 168, 106–111. doi: 10.1016/j.jseaes.2017.10.022

Liang, Q., Hu, Y., Feng, D., Peckmann, J., Chen, L., Yang, S., et al. (2017). Authigenic carbonates from newly discovered active cold seeps on the northwestern slope of the south China Sea: Constraints on fluid sources, formation environments, and seepage dynamics. *Deep Sea Res. Part I: Oceanographic Res. Papers* 124, 31–41. doi: 10.1016/j.dsr.2017.04.015

Lim, Y. C., Lin, S., Yang, T. F., Chen, Y. G., and Liu, C. S. (2011). Variations of methane induced pyrite formation in the accretionary wedge sediments offshore southwestern Taiwan. *Mar. Petrology Geol.* 28, 1829–1837. doi: 10.1016/j.marpetgeo.2011.04.004

Lin, Q., Wang, J., Taladay, K., Lu, H., Hu, G., Sun, F., et al. (2016). Coupled pyrite concentration and sulfur isotopic insight into the paleo sulfate–methane transition zone (SMTZ) in the northern south China Sea. *J. Asian Earth Sci.* 115, 547–556. doi: 10.1016/j.jseaes.2015.11.001

Lisiecki, L. E., and Raymo, M. E. (2005). A pliocene-pleistocene stack of 57 globally distributed benthic δ18O records. *Paleoceanography* 20. doi: 10.1029/2004PA001071

Liu, S., Feng, X., Feng, Z., Xiao, X., and Feng, L. (2020). Geochemical evidence of methane seepage in the sediments of the qiongdongnan basin, south China Sea. *Chem. Geol.* 543, 119588. doi: 10.1016/j.chemgeo.2020.119588

Liu, E. T., Wang, H., Pan, S. Q., Qin, C. Y., Jiang, P., Chen, S., et al. (2021). Architecture and depositional processes of sublacustrine fan systems in structurally active settings: An example from weixinan depression, northern south China Sea. *Mar. Petroleum Geol.* 134, 105380. doi: 10.1016/j.marpetgeo.2021.105380

Lombo Tombo, S., Dennielou, B., Berné, S., Bassetti, M. A., Toucanne, S., Jorry, S. J., et al. (2015). Sea-Level control on turbidite activity in the Rhone canyon and the upper fan during the last glacial maximum and early deglacial. *Sedimentary Geol.* 323, 148–166. doi: 10.1016/j.sedgeo.2015.04.009

Maloney, J. M., Bentley, S. J., Xu, K., Obelcz, J., Georgiou, I. Y., Jafari, N. H., et al. (2020). Mass wasting on the Mississippi river subaqueous delta. *Earth-Science Rev.* 200, 103001. doi: 10.1016/j.earscirev.2019.103001

Maslin, M., Mikkelsen, N., Vilela, C., and Haq, B. (1998). Sea-Level –and gas-hydrate–controlled catastrophic sediment failures of the Amazon fan. *Geology* 26, 1107–1110. doi: 10.1130/0091-7613(1998)0262.3.CO;2

Masson, D. G. (1996). Catastrophic collapse of the volcanic island of hierro 15 ka ago and the history of landslides in the canary islands. *Geology* 24, 231–234. doi: 10.1130/0091-7613(1996)0242.3.CO;2

Miao, X., Feng, X., Li, J., and Lin, L. (2021a). Tracing the paleo-methane seepage activity over the past 20,000 years in the sediments of qiongdongnan basin, northwestern south China Sea. *Chem. Geol.* 559, 119956. doi: 10.1016/j.chemgeo.2020.119956

Miao, X., Feng, X., Li, J., Liu, X., Liang, J., Feng, J., et al. (2022). Enrichment mechanism of trace elements in pyrite under methane seepage. *Geochem. Perspect. Lett.* 21, 18–22. doi: 10.7185/geochemlet.2211

Miao, X., Feng, X., Liu, X., Li, J., and Wei, J. (2021b). Effects of methane seepage activity on the morphology and geochemistry of authigenic pyrite. *Mar. Petroleum Geol.* 133, 105231. doi: 10.1016/j.marpetgeo.2021.105231

Mienert, J., Vanneste, M., Bünz, S., Andreassen, K., Haflidason, H., and Sejrup, H. P. (2005). Ocean warming and gas hydrate stability on the mid-Norwegian margin at the storegga slide. *Mar. Petroleum Geol.* 22, 233–244. doi: 10.1016/j.marpetgeo.2004.10.018

Nisbet, E. G., and Piper, D. J. W. (1998). Giant submarine landslides. *Nature* 392, 329–330. doi: 10.1038/32765

Passega, R. (1957). Texture as characteristic of clastic deposition. *AAPG Bull.* 41, 1952–1984. doi: 10.1306/0BDA594E-16BD-11D7-8645000102C1865D

Passega, R. (1977). Significance of CM diagrams of sediments deposited by suspensions. *Sedimentology* 24, 723–733. doi: 10.1111/j.1365-3091.1977.tb00267.x

Paull, C. K., Buelow, W. J., Ussler, W., and Borowski, W. S. (1996). Increased continental-margin slumping frequency during sea-level lowstands above gas hydrate–bearing sediments. *Geology* 24, 143–146. doi: 10.1130/0091-7613(1996)024<0143: ICMSFD>2.3.CO;2

Paull, C. K., Ussler Iii, W., and Dillon, W. P. (1991). Is the extent of glaciation limited by marine gas-hydrates? *Geophys. Res. Lett.* 18, 432–434. doi: 10.1029/91GL00351

Peckmann, J., Thiel, V., Reitner, J., Taviani, M., Aharon, P., and Michaelis, W. (2004). A microbial mat of a Large sulfur bacterium preserved in a Miocene methane-seep limestone. *Geomicrobiol. J.* 21, 247–255. doi: 10.1080/01490450490438577

Peketi, A., Mazumdar, A., Joshi, R. K., Patil, D. J., Srinivas, P. L., and Dayal, A. M. (2012). Tracing the paleo sulfate-methane transition zones and H2S seepage events in marine sediments: An application of c-S-Mo systematics. *Geochem. Geophys. Geosystems* 13. doi: 10.1029/2012GC004288

Phrampus, B. J., and Hornbach, M. J. (2012). Recent changes to the gulf stream causing widespread gas hydrate destabilization. *Nature* 490, 527–530. doi: 10.1038/nature11528

Pouderoux, H., Proust, J.-N., Lamarche, G., Orpin, A., and Neil, H. (2012). Postglacial (after 18ka) deep-sea sedimentation along the hikurangi subduction margin (New zealand): Characterisation, timing and origin of turbidites. *Mar. Geol.* 295-298, 51–76. doi: 10.1016/j.margeo.2011.11.002

Prins, M. A., and Postma, G. (2000). Effects of climate, sea level, and tectonics unraveled for last deglaciation turbidite records of the Arabian Sea. *Geology* 28, 4. doi: 10.1130/0091-7613(2000)282.0.CO;2

Reagan, M. T., and Moridis, G. J. (2007). Oceanic gas hydrate instability and dissociation under climate change scenarios. *Geophys. Res. Lett.* 34. doi: 10.1029/2007GL031671

Rothwell, R. G., Thomson, J., and Kähler, G. (1998). Low-sea-level emplacement of a very large late pleistocene 'megaturbidite' in the western Mediterranean Sea. *Nature* 392, 377–380. doi: 10.1038/32871

Sato, H., Hayashi, K., Ogawa, Y., and Kawamura, K. (2012). Geochemistry of deep sea sediments at cold seep sites in the nankai trough: Insights into the effect of anaerobic oxidation of methane. *Mar. Geol.* 323-325, 47–55. doi: 10.1016/j.margeo.2012.07.013

Schmidt, F., Schmidt, A., Treguier, E., Guiheneuf, M., Moussaoui, S., and Dobigeon, N. (2010). Implementation strategies for hyperspectral unmixing using Bayesian source separation. *IEEE Trans. Geosci. Remote Sens.* 48, 4003–4013. doi: 10.1109/TGRS.2010.2062190

Shackleton, N. J. (1987). Oxygen isotopes, ice volume and sea level. *Quaternary Sci. Rev.* 6, 183–190. doi: 10.1016/0277-3791(87)90003-5

Tong, H., Feng, D., Cheng, H., Yang, S., Wang, H., Min, A. G., et al. (2013). Authigenic carbonates from seeps on the northern continental slope of the south China Sea: New insights into fluid sources and geochronology. *Mar. Petroleum Geol.* 43, 260–271. doi: 10.1016/j.marpetgeo.2013.01.011

Toucanne, S., Zaragosi, S., Bourillet, J. F., Naughton, F., Cremer, M., Eynaud, F., et al. (2008). Activity of the turbidite levees of the celtic–armorican margin (Bay of Biscay) during the last 30,000 years: Imprints of the last European deglaciation and Heinrich events. *Mar. Geol.* 247, 84–103. doi: 10.1016/j.margeo.2007.08.006

Waelbroecka, C., Labeyrie, L., Michel, E., Duplessy, J. C., McManus, J. F., Lambeck, K., et al. (2002). Sea-Level and deep water temperature changes derived from benthic foraminifera isotopic records.pdf. *Quaternary Sci. Rev.* 21, 11. doi: 10.1016/S0277-3791 (01)00101-9

Wan, S., and Jian, Z. (2014). Deep water exchanges between the south China Sea and the pacific since the last glacial period. *Paleoceanography* 29, 1162–1178. doi: 10.1002/2013PA002578

Wang, G., Xie, S.-P., Qu, T., and Huang, R. X. (2011). Deep south China Sea circulation. *Geophys. Res. Lett.* 38, L05601. doi: 10.1029/2010GL046626

Wang, S. H., Song, H. B., and Yan, W. (2004). Environmental effects of natural gas hydrate. *Bulletin of Mineralogy Petrology and Geochemistry* 23 (2), 160–165. doi: 10.1038/nature14399

Wei, W., and Algeo, T. J. (2020). Elemental proxies for paleosalinity analysis of ancient shales and mudrocks. *Geochimica Cosmochimica Acta* 287, 341–366. doi: 10.1016/j.gca.2019.06.034

Wei, J., Wu, T., Zhang, W., Deng, Y., Xie, R., Feng, J., et al. (2020). Deeply buried authigenic carbonates in the qiongdongnan basin, south China Sea: Implications for ancient cold seep activities. *Minerals* 10. doi: 10.3390/min10121135

Yang, K., Chu, F., Zhu, Z., Dong, Y., Yu, X., Zhang, W., et al. (2018). Formation of methane-derived carbonates during the last glacial period on the northern slope of the south China Sea. *J. Asian Earth Sci.* 168, 173–185. doi: 10.1016/j.jseaes.2018.01.022

Yu, S.-W., Tsai, L. L., Talling, P. J., Lin, A. T., Mii, H.-S., Chung, S.-H., et al. (2017). Sea Level and climatic controls on turbidite occurrence for the past 26kyr on the flank of the gaoping canyon off SW Taiwan. *Mar. Geol.* 392, 140–150. doi: 10.1016/j.margeo.2017.08.011

Zaragosi, S., Bourillet, J.-F., Eynaud, F., Toucanne, S., Denhard, B., Van Toer, A., et al. (2006). The impact of the last European deglaciation on the deep-sea turbidite systems of the celtic-armorican margin (Bay of Biscay). *Geo-Marine Lett.* 26, 317–329. doi: 10.1007/s00367-006-0048-9

Zhang, J., Lei, H., Chen, Y., Kong, Y., Kandasamy, S., Ou, W., et al. (2018b). Carbon and oxygen isotope composition of carbonate in bulk sediment in the southwest Taiwan basin, south China Sea: Methane hydrate decomposition history and its link to mud volcano eruption. *Mar. Petroleum Geol.* 98, 687–696. doi: 10.1016/j.marpetgeo.2018.08.031

Zhang, Y., Liu, Z., Zhao, Y., Colin, C., Zhang, X., Wang, M., et al. (2018a). Long-term *in situ* observations on typhoon-triggered turbidity currents in the deep sea. *Geology* 46, 675–678. doi: 10.1130/G45178.1

Zhang, K., Song, H., Tao, J., Wang, H., and Geng, M. (2020). A preliminary study on the active cold seeps flow field in the qiongdongnan Sea area, the northern south China Sea. *Chin. Sci. Bull.* 65, 1130–1140. doi: 10.1360/TB-2019-0582

Zhao, Y., Liu, Z., Colin, C., Xie, X., and Wu, Q. (2011). Turbidite deposition in the southern south China Sea during the last glacial: Evidence from grain-size and major elements records. *Chin. Sci. Bull.* 56, 3558–3565. doi: 10.1007/s11434-011-4685-7

Zhao, Y., Liu, Z., Zhang, Y., Li, J., Wang, M., Wang, W., et al. (2015). *In situ* observation of contour currents in the northern south China Sea: Applications for deepwater sediment transport. *Earth Planetary Sci. Lett.* 430, 477–485. doi: 10.1016/j.epsl.2015.09.008

Zhou, C., Zhao, W., Tian, J., Zhao, X., Zhu, Y., Yang, Q., et al. (2017). Deep Western boundary current in the south China Sea. *Sci. Rep.* 7, 9303. doi: 10.1038/s41598-017-09436-2

Zhu, Y., Sun, J., Wang, Y., Li, S., Xu, T., Wei, Z., et al. (2019). Overview of the multi-layer circulation in the south China Sea. *Prog. Oceanogr.* 175, 171–182. doi: 10.1016/j.pocean.2019.04.001